Heliyon 9 (2023) e22038

Contents lists available at ScienceDirect

Heliyon

journal homepage: www.cell.com/heliyon

Novel g-C_3N_4/$PrFeO_3$ nanocomposites with Z-scheme structure and superior photocatalytic activity toward visible-light-driven removal of tetracycline antibiotics

M.I. Chebanenko [a,*], L.A. Lebedev [a], A.S. Seroglazova [a], A.A. Lobinsky [a], E.Y. Gerasimov [b], E. Yu Stovpiaga [a], V.I. Popkov [a]

[a] *Ioffe Institute, St. Petersburg, 194021, Russia*
[b] *Boreskov Institute of Catalysis SB RAS, Novosibirsk, 630090, Russia*

ARTICLE INFO

Keywords:
G-C_3N_4
$PrFeO_3$
Photocatalytic degradation
Tetracycline hydrochloride
Z-scheme heterojunction

ABSTRACT

In the presented work, heterostructured nanocomposites based on g-C_3N_4 and $PrFeO_3$ with different mass content of $PrFeO_3$ (0–10 wt%) were prepared by ultrasonic processing to study their photocatalytic activity in the process of antibiotic degradation under visible light. The study of phase composition, structural, morphological and textural characteristics carried out by powder X-ray diffraction, scanning electron microscopy and adsorption-structural analysis confirmed the presence of two phases - graphite-like C_3N_4 and orthorhombic $PrFeO_3$ with average crystallite sizes of 5 and 21 nm and mesoporous structure with specific surface area of 57.2–68.6 m^2/g and average pore size of 20 nm. The measured values of the forbidden bandwidth for the obtained nanocomposites were ~3 eV, indicating potential activity under visible light irradiation. The efficiency of antibiotic removal under visible light was evaluated in the degradation of TCHCl. It was found that 5 % $PrFeO_3$ content was optimal and increased the TOF by 5 times compared to pure g-C_3N_4. The results of photocatalytic test with absorbers showed that photocatalysis occurs by Z-scheme mechanism. The results obtained allow us to consider this nanocomposite as an effective and stable photocatalyst for pharmaceutical wastewater treatment.

1. Introduction

The constant increase in the consumption of medicines in the absence of proper disposal control measures inevitably leads to negative consequences for the environment. The production of medicines is a multi-stage process. At each stage, wastewater with a variable content of mineral and organic substances is generated [1,2]. Sewage treatment plants are incapable of effectively removing these substances from wastewater. The ingress of pharmaceuticals into aquatic ecosystems leads to unpredictable consequences and has a negative impact on living organisms. As a consequence, interest in the problem of treating industrial wastewater from such compounds has been growing rapidly [3–5].

To date, the photocatalytic oxidation of pharmaceutical compounds is considered one of the most promising areas for solving the issue of industrial wastewater treatment. Particularly, the acceleration of the chemical reaction of pollutant decomposition is achieved by the combined actions of catalyst and light irradiation [6]. The viability of this method relies on the possibility of unlimited use of

* Corresponding author.
E-mail address: m_chebanenko@list.ru (M.I. Chebanenko).

https://doi.org/10.1016/j.heliyon.2023.e22038
Received 3 June 2023; Received in revised form 31 October 2023; Accepted 2 November 2023
Available online 7 November 2023

solar energy. In this regard, the search and development of effective photocatalysts is an important task that concentrates on the ability of the material to create electron-hole pairs under the influence of visible light.

In the last decade, graphite-like carbon nitride (g-C_3N_4) has attracted the attention of researchers due to its high photoactivity and effective absorption of visible light. The main method of obtaining g-C_3N_4 in the form of nanopowders is the thermolysis of various organic precursors (melamine, urea, thiourea, and dicyandiamide) [7]. Despite the large number of precursors, urea is most commonly used, as it achieves the highest values of the specific surface area of the product under the same conditions of synthesis [8,9]. Graphite-like carbon nitride is a two-dimensional sheet that has a hexagonal structure based on tri-*c*-triazine links [10]. The presence of nitrogen atoms in the graphite-like layered structure gives it unique semiconductor properties and the ability to absorb radiation in the visible region of the spectrum (band gap width 2.7–3.1 eV) [11]. Thus, g-C_3N_4 consists of widely distributed chemical elements and exhibits high photocatalytic activity in processes induced by the activity of visible radiation [12]. However, the photocatalytic capabilities of primordial g-C_3N_4 are low due to the high recombination rate of charge carriers and insufficient specific surface area. To overcome these shortcomings, various methods of modification of g-C_3N_4 are studied and developed.

One of the promising but little-studied areas is the fabrication of heterostructures based on nanocrystalline graphite-like carbon nitride (g-C_3N_4) and orthoferrites of rare-earth elements ($RFeO_3$, R=Sc, Y, Ln). Due to the effective spatial separation of photogenerated electrons and holes, the speed of the photocatalytic reaction increases significantly [13,14]. In addition, the absorption band of such composite materials can be increased since the semiconductors in their composition have different band gap widths.

A large number of studies focus on the study of perovskite-like orthoferrites of rare earth elements due to the wide range of their functional applications as a basis for new materials for sensors, gas separators, electromagnetic devices, and photocatalysis [15–17]. One of the most photoactive orthoferrites of rare-earth elements is praseodymium orthoferrite ($PrFeO_3$), which has high photocatalytic activity when exposed to visible light in addition to its outstanding electromagnetic properties. However, early studies of its catalytic properties are limited due to the single disadvantage of reduced catalytic activity during processes of reverse recombination of electron-hole pairs [18–21]. One of the methods to suppress the processes of reverse recombination is to create a heterojunction structure by adding a second component to the main phase. Its presence allows for the transfer of charge carriers immediately after the formation of an electron-hole pair [22–25]. Earlier studies have indicated that photocatalytic systems with heterojunction based on $PrFeO_3$ can demonstrate improved catalytic characteristics by including semiconductor catalysts based on CeO_2, TiO_2, and ZnO [22,23,26]. A larger value of the band gap width reduces the recombination time of electron-hole pairs and increases the surface area.

In this study, heterostructural photoactive nanocomposites based on g-C_3N_4 and $PrFeO_3$ were obtained for the first time using ultrasonic dispersion of powders in ethanol. The composition of the nanocomposite was optimized by changing the mass fraction of $PrFeO_3$ in the graphite-like carbon nitride powder. The resulting series was characterized by various physico-chemical methods. The catalytic activity of g-C_3N_4/$PrFeO_3$ was evaluated during the photocatalytic decomposition of tetracycline hydrochloride (TCHCl) under the influence of visible radiation. In the final part of the work, a photocatalytic experiment in the presence of scavenging agents was proposed, which enabled us to infer the mechanism of the resulting Z-scheme.

2. Experimental

2.1. Materials

Urea (99.8 %, CH_4N_2O), praseodymium trinitrate hexahydrate (99.9 %, $Pr(NO_3)_3{\cdot}6H_2O$), iron (III) nitrate nonahydrate (98.0 %, $Fe(NO_3)_3{\cdot}9H_2O$), glycine (99.5 %, $C_2H_5NO_2$), ascorbic acid (99.0 %, $C_6H_8O_6$), formic acid (85.0 %, CH_2O_2), were purchased from NevaReaktiv. Tetracycline hydrochloride (95 %, $C_{22}H_{24}N_2O_8{\cdot}HCl$) was obtained from neoFroxx. All the reagents used in this research work are analytical grade. Deionized water is obtained from the analytical laboratory.

2.2. Synthesis of g-C_3N_4

The initial graphite-like carbon nitride powder was obtained by the thermal polymerization of urea (CH_4N_2O). The heating rate of the muffle furnace was 5°/min, the heat treatment temperature was 550°C, the holding time was 2 h, and the heat treatment was carried out in an air atmosphere [27,28]. The yield of carbon nitride relative to the initial urea as a result of its heat treatment in air is about 2 wt% [29].

2.3. Synthesis of $PrFeO_3$

Nanopowders based on praseodymium orthoferrite ($PrFeO_3$) were obtained by solution combustion with a glycine-nitrate ratio of G/N = 2.0. Aqueous nitrates of the corresponding metals $Pr(NO_3)_3{\cdot}6H_2O$ and $Fe(NO_3)_3{\cdot}9H_2O$ were used as starting reagents, and glycine ($C_2H_5NO_2$) was used as fuel. The number of initial reagents was calculated using the reaction equation:

$$3Pr(NO_3)_3 + 3Fe(NO_3)_3 + 10C_2H_5NO_2 = 3PrFeO_3 + 20CO_2 + 14\ N_2 + 25H_2O$$

During the synthesis of praseodymium nitrate, iron (III) nitrate and glycine were dissolved in 30 ml of distilled water with constant stirring until all reagents were completely dissolved. The prepared reaction mixture was heated on an electric laboratory burner until complete evaporation of water and subsequent spontaneous combustion. The resulting foamy product was additionally crushed in a mortar until a homogeneous powder was formed and annealed at 700°C for 1 h to completely remove unreacted components and form

crystalline $PrFeO_3$.

2.4. Synthesis of g-C_3N_4/$PrFeO_3$ nanocomposite

The initial graphite-like carbon nitride powder was subjected to ultrasonic exfoliation in ethyl alcohol (C_2H_5OH) for 2 h. Five portions of a suspension containing 30 ml of C_2H_5OH and 0.5 g of g-C_3N_4 were prepared. A predetermined amount of praseodymium ferrite powder (2.5, 5, 7.5, and 10 wt%) was added to the suspension, treated with ultrasound for another 2 h, and finally dried for 4 h at 80 °C until the ethyl alcohol was completely removed. Pure samples of g-C_3N_4 (hereinafter CN) and $PrFeO_3$ (hereinafter PFO) were obtained analogically. Sample series of CN, PFO, CN/2.5 % PFO, CN/5 % PFO, CN/7.5 % PFO, and CN/10 % PFO were investigated using a complex of physicochemical analysis methods.

2.5. Physicochemical characterization

The crystal structure of the powders was studied using a Rigaku SmartLAB III diffractometer (CuKα radiation, λ = 0.154051 nm) in the range of 10–60°(2θ). The average size of the crystallites was estimated using Debye-Scherrer's equation (1):

$$D = \frac{0.94 \bullet \lambda}{\beta \bullet \cos\theta} \tag{1}$$

where λ is the wavelength of the incident radiation (CuK $\alpha = 0.154$ nm); β is the full width at half maximum in radians; θ is the Bragg angle in radians.

The morphology of the samples was obtained using a Tescan Mira scanning electron microscope equipped with a Standard Aztec Energy/X-act energy-dispersive X-ray (EDX) analyzer.

The transmission electron microscopy (TEM) studies and elemental mapping carried out using a Hitachi HT7700 TEM with an acceleration voltage of 100 kV, W source.

The Brunauer-Emmett-Teller (BET) surface area was measured by a Micromeritics 3Flex surface area analyzer. The pore size distribution plots were generated from a desorption branch of the isotherm by the Barrett-Joyner-Halenda (BJH) method.

Diffuse reflection spectra and photoluminescence spectra were recorded using an Avaspec-ULS2048CL-EVO spectrometer equipped with an AvaSphere-30-REFL refractometric integration sphere in the 350–700 nm region. The obtained diffuse reflection spectra were transformed using the Kubelka-Munk function to estimate the energy of the band gap. The reflection coefficient $F(R)$ was calculated using formula (2):

$$F(R) = \frac{(1-R)^2}{2R} \tag{2}$$

where R is the reflectance [30].

X-ray photoelectron spectroscopy (XPS) spectra were found using Thermo Fisher Scientific Escalab 250Xi complex spectrometer.

2.6. Photocatalytic activity

Tetracycline hydrochloride (TCHCl) was chosen as a model antibiotic. The concentration of TCHCl in the initial solution was 0.03 g/l. The pH of the solution was 6.5. The catalyst powder (1 mg) was thoroughly dispersed in the initial antibiotic solution and placed in a photocatalytic reactor cuvette. The capacity of the cuvette was 10 ml. The solution was then stirred in the dark for 1 h to achieve an adsorption-desorption equilibrium. Next, the solution was irradiated with LEDs (power consumption: 24 W, $\lambda_{max} = 405$ nm) and continuously stirred under the influence of visible radiation. The measurements were carried out in-situ using an Avaspec-ULS2048CL-EVO spectrometer equipped with an Avalight-XE Pulsed Xenon Lamp.

The degree of decomposition of the antibiotic under the influence of visible radiation in the presence of a catalyst was determined by formula (3):

$$\text{Rem.Eff.} = \frac{(C_0 - C)}{C_0} \bullet 100\% \tag{3}$$

where C_0 is the concentration of the initial TCHCl solution and C is the concentration of the TCHCl solution after exposure to light.

The efficiency of the photocatalysts was evaluated using the turnover number (TON) and the turnover frequency (TOF). TON represents the maximum yield of products achieved in the active catalytic center, up to a decrease in activity for a specific reaction, and can be calculated using equation (4):

$$TON = \frac{Rem.Eff. \bullet (Moles\ of\ TCHCl)}{Moles\ of\ catalyst} \tag{4}$$

The turnover frequency (TOF), indicating how many times the catalytic cycle occurs at one site per unit of time, was determined as the number of reaction products formed at one active site per unit of time (5):

$$TOF = \frac{TON}{Reaction\ time} \quad (5)$$

The stability of the most active photocatalyst was investigated using a cyclic photocatalytic degradation test of an aqueous solution of TCHCl under visible light irradiation. The powder was collected, washed between the cycles of photocatalysis, and then returned to the reactor with the initial concentration of the antibiotic.

To better understand the mechanism of photocatalytic decomposition using the obtained catalysts, an experiment was conducted in the presence of various scavenging agents. 0.1 mM of isopropyl alcohol (IPA), ascorbic acid (AA) and formic acid (FA) were used as absorbers of hydroxyl radicals (·OH), superoxide radicals ($\cdot O^{2-}$), and holes (h^+), respectively. The concentrations of the antibiotic and catalyst in the experiment were 0.005 g/l and 0.1 g/l, respectively, and were selected based on literature data [31].

3. Results and discussion

3.1. Powder X-ray diffraction

The results of powder X-ray diffraction are shown in Fig. 1a. The analysis showed that the CN sample is single-phase and corresponds to JCPDS card No. 87–1526. The pattern is represented by two reflexes typical for graphite-like carbon nitride at Bragg angles of ~12.5 and 27.1°, which results from the repeating of tri-*c*-triazine links in the plane and the ordering of conjugated aromatic rings in the structure of graphite-like carbon nitride, respectively. Patterns of nanocomposites contain peaks belonging to both CN and PFO. At the same time, there is no pronounced displacement of reflexes when the ratio of the initial components varies. The intensity of the peaks belonging to PFO naturally increases with an increase in the mass fraction of praseodymium orthoferrite in the nanocomposite. Annealed PFO nanoparticles have an orthorhombic structure of the *Pnma* spatial group without secondary phases. Fig. 1b shows that the observed PFO reflexes are in good agreement with JCPDS standards and correspond to card No. 02–7274.

The size distribution of the crystallites is shown in Fig. 1c. The average size of the crystallites was determined by the broadening of the most intense reflex (002) and (112) for CN and PFO and was 5 ± 0.5 nm and 21 ± 1 nm, respectively.

3.2. X-ray photoelectron spectroscopy

Fig. 2a illustrates the X-ray spectrum in which peaks were observed for C 1s, N 1s, Pr 3d, Fe 2p and O 1s of the CN/5 % PFO photocatalyst. Deconvolution of the carbon spectrum (Fig. 2b) reveals three peaks at 284.2 eV, 288.7 eV and 286.1 eV, which belong to the C–C, $(C)_3$–N and C–N–C bonds, respectively [32]. The dominant peak at 399.3 eV (Fig. 2c) is assigned to the tertiary N bonded to C atoms in the form of N-$(C)_3$ [33]. Fig. 2d shows the spectrum of praseodymium. The peak positions at 933.0 eV and 953.4 eV can be attributed to Pr $3d_{5/2}$ and Pr $3d_{3/2}$, while 928.5 eV and 948.1 eV are satellite peaks. The spectrum of iron is shown in Fig. 2e. The binding energy at 711.1 eV and 724.6 eV belongs to Fe $2p_{3/2}$ and $2p_{1/2}$ with an oxidation state of 2+ [34]. The peak at 718.9 eV is satellite. The oxygen spectrum revealed the presence of two peaks (Fig. 2f). The binding energy of 529.7 eV belongs to oxygen located

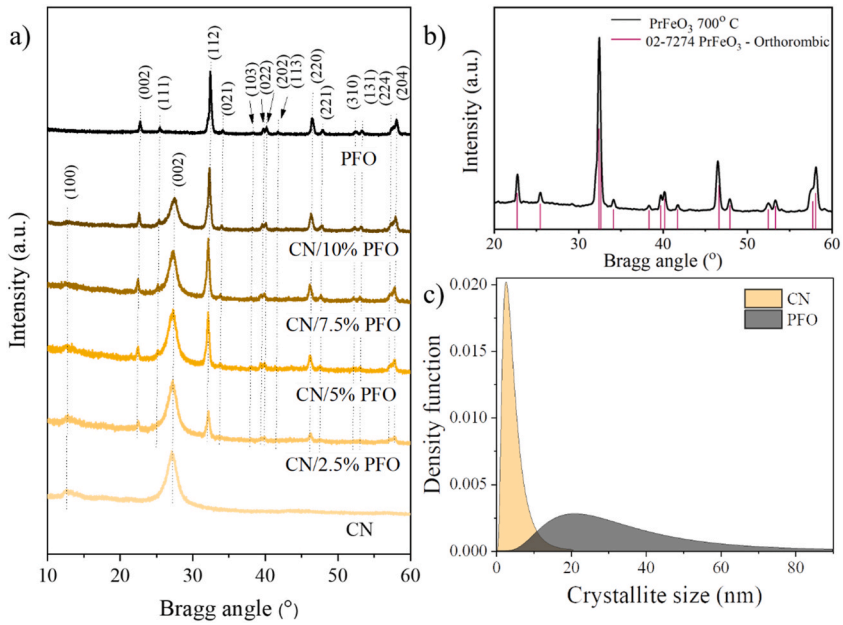

Fig. 1. X-ray diffraction patterns of CN, PFO and CN/PFO nanocomposites (a), standard (JCPDS #02–7274) and synthesized $PrFeO_3$ (b) and crystallite size distribution of the CN and PFO of CN/5%PFO nanocomposite (c).

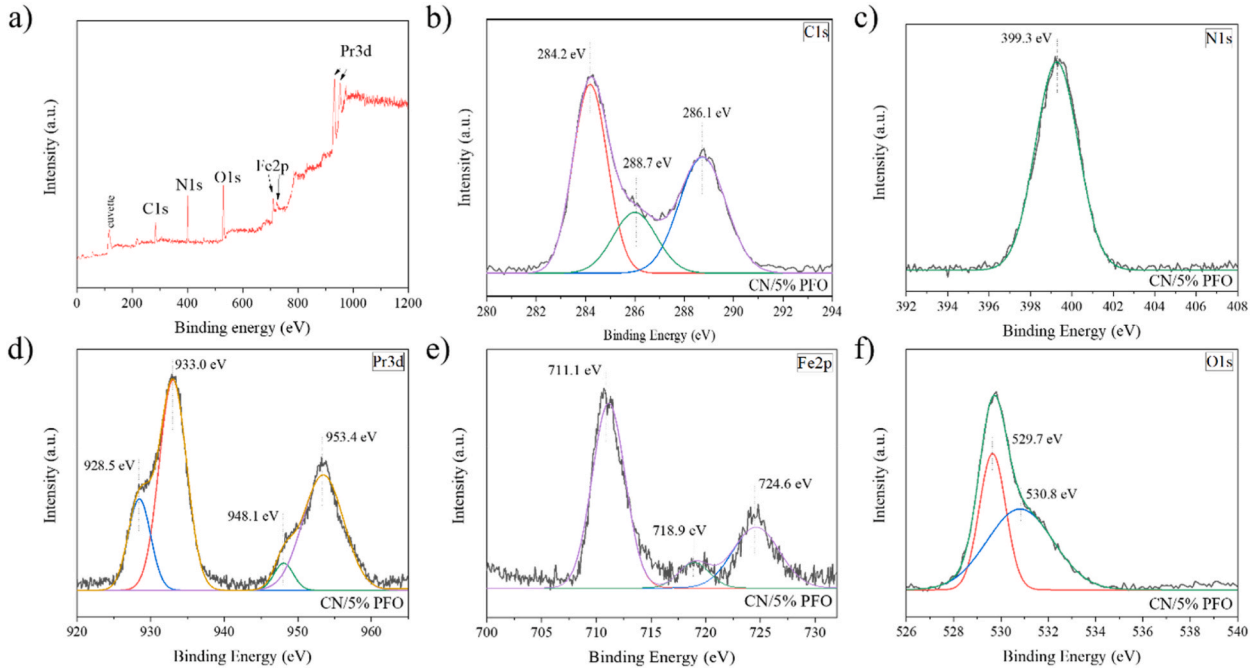

Fig. 2. The XPS survey of CN/5 % PFO (a); the fine spectra of XPS analysis for C (b), N (c), Pr (d), Fe (e) and O (f) elements.

in the $PrFeO_3$ crystal lattice. The peak at 530.8 eV belongs to the adsorbed on the surface. The results obtained are in good agreement with the literature data describing the g-C_3N_4 and $PrFeO_3$ spectra.

3.3. Scanning and transmission electron microscopies

SEM images were obtained to consider the shape and spatial organization of the obtained powders. The morphology typical for graphite-like carbon nitride is represented by "crumpled" two-dimensional sheets with a high degree of agglomeration (Fig. 3 a, b). The PFO sample has a foam-like morphology (Fig. 3 k, l). The formation of the foamy structure is caused by the abundant release of gaseous products by solution combustion during the synthesis. SEM images of the resulting nanocomposites are shown in Fig. 3 c-j. It is shown that the quantity of orthoferrite crystal particles distributed over the surface of g-C_3N_4 increases with an increase in the mass fraction of PFO in the nanocomposite. The deposition of a large number of crystalline PFO particles with an average diameter of ~20 nm on the CN surface confirms the X-ray diffraction data (Fig. 1 c). Notably, some PFO particles are represented as agglomerates consisting of dozens of particles (Fig. 3 f).

The element mapping of a typical CN/5%PFO nanocomposite is shown in Fig. 4 a-f. This method allowed to control the chemical purity of the obtained catalysts and evaluate the uniformity of the distribution of elements over the sample. The analysis proved the existence exclusively of the anticipated elements such as C, N, Pr, Fe, and O without any impurities. The homogeneous distribution of elements in the composite was also confirmed.

Morphology of CN, PFO and CN/5%PFO nanocomposite was studied with TEM microscopy, images are shown on Fig. 5. Pristine graphite-like C_3N_4 appears as assembly of ragged-edged two-dimensional nanosheets (Fig. 5 a). Mesoporous structure can be revealed at higher magnification (Fig. 5 b), these pores are formed upon thermopolymerization reaction of urea due to evolution of large amount of gases. Praseodymium orthoferrite structure shown on Fig. 5c and d, it is clearly seen that its foam-like consistency, that produced due to synthetic rout, assembled from a number of separate irregular-shaped particles. Under ultrasonic treatment PFO particles distributed on the surface of CN sheets in a random manner as shown on Fig. 5 e, f. To further verify PFO content in composites, elemental mapping of CN/5%PFO was used (Fig. 5 g, h).

3.4. Low-temperature nitrogen adsorption/desorption studies

The surface and porosity of the samples were studied by low-temperature adsorption-desorption of nitrogen. Typical isotherms of IV type with pronounced hysteresis of H3 type were obtained, which indicates the presence of mesopores in the studied catalysts (Fig. 6a). The values of the specific surface area were obtained by the BET method and are shown in the form of a bar chart in Fig. 6b. It is shown that the addition of PFO to graphite-like carbon nitride leads to an increase in the values of the specific surface area of the sample.

The positive effect of ultrasonic exposure on the value of the specific surface area CN was previously demonstrated in the work [27, 28]. It was proved that this procedure allows to reduce the agglomeration of two-dimensional CN layers and significantly increase the

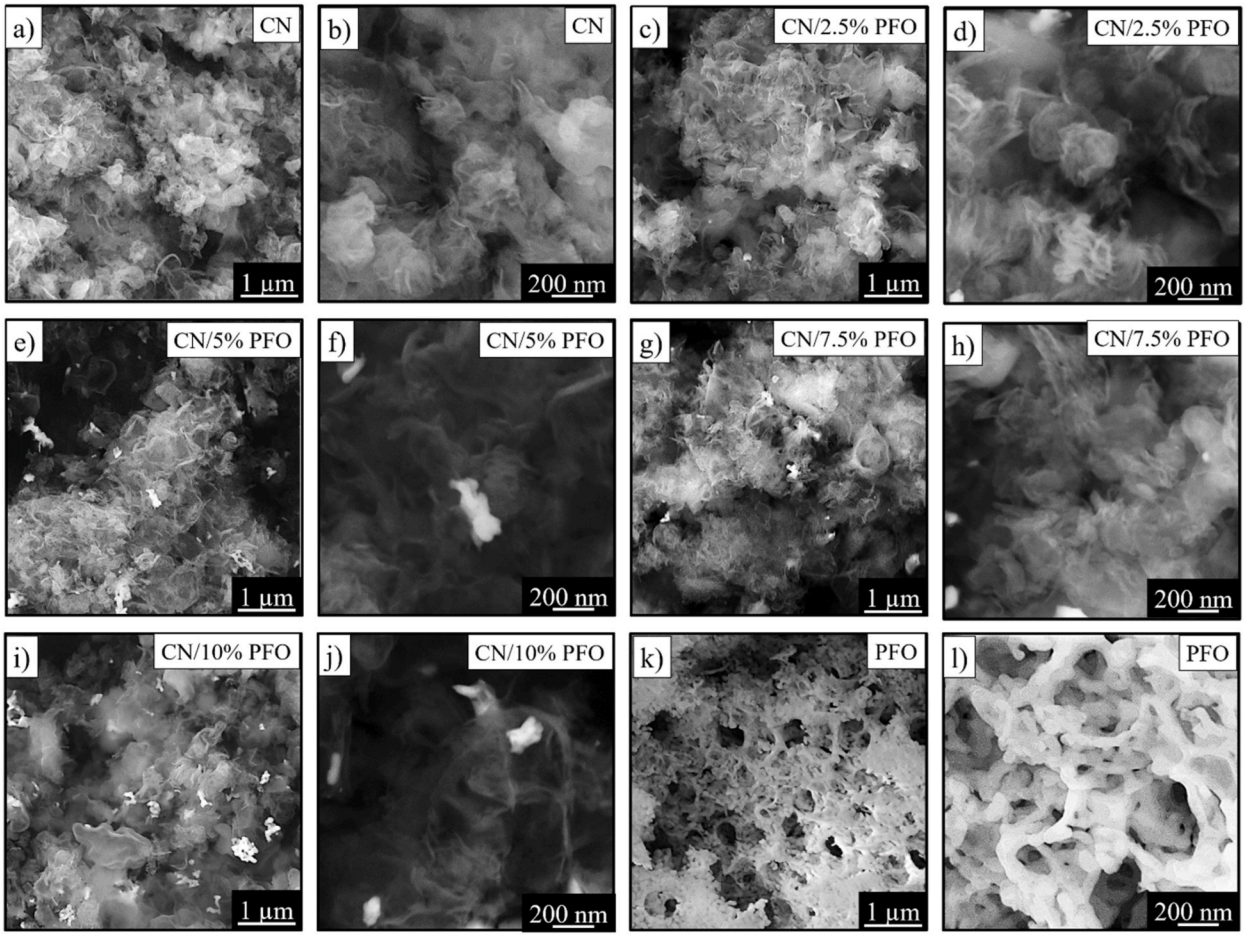

Fig. 3. SEM images of the CN (a–b), CN/2.5%PFO (c–d), CN/5%PFO (e–f), CN/7.5%PFO (g–h), CN/10%PFO (i–j) and PFO (k–l) nanopowders.

available surface of the sample due to effective exfoliation. Thus, a consistent increase in the values of the specific surface area of nanocomposites is caused by ultrasonic exposure, as well as the introduction of the orthoferrite praseodymium additive. Presumably, under the influence of ultrasound, PFO particles penetrate between the CN layers and prevent re-agglomeration. The theoretically predicted curve shown in Fig. 6b is based on the assumption that when a given amount of additive is introduced, PFO does not penetrate into the interlayer space but is located on the surface of the stacks, which leads to a decrease in the values of the specific surface area due to the overlap of the CN surface available for adsorption.

The BJH pore size distribution graph (Fig. 6c) shows that the obtained materials have a pore size distribution in the range from 2 to 100 nm, which also confirms the mesoporous structure of the obtained catalysts. The average pore size for nanocomposites was 20 ± 2 nm (Table S1). Effectively, such a developed porous structure and high specific surface area can have a positive effect on the separation efficiency of light-generated electrons and holes.

3.5. Ultraviolet–visible (UV–vis) and photoluminescence spectroscopies

Diffuse reflection spectra in the UV–visible region were obtained to consider the electronic structure of the samples. As shown in Fig. 7a, initial CN showed an absorption edge located at a wavelength of 413 nm, while the PFO spectrum exhibited a stronger absorption edge located at 566 nm. Therefore, a quantum-dimensional effect of the "red" shift type is observed with the introduction of a PFO additive. This means that the edge of the absorption band is shifted to the long-wavelength region, and a lower energy of the absorbed quantum is required to excite electrons from the valence band to the conduction band. The band gap width (E_g) was determined using the Kubelka-Munk function by the linear extrapolation of the inclined part of the spectrum to the intersection with the abscissa axis (Fig. 7b). The calculated band gap energies for pure CN and pure PFO were 2.19 eV and 3.0 eV, respectively.

Photoluminescence spectra of prepared samples at 365 nm excitation shown on Fig. 7 c, integral luminescence intensity for all samples also presented on Fig. 7 d, pure PFO doesn't show any signs of luminescence in visible region. It was shown that the spectra are less intense for all PFO decorated samples compared to pristine CN, as well as significant drop in intensity for most catalytically active sample, due to lower rate of radiative recombination related to generation of active oxygen species thus attributed to photocatalytic

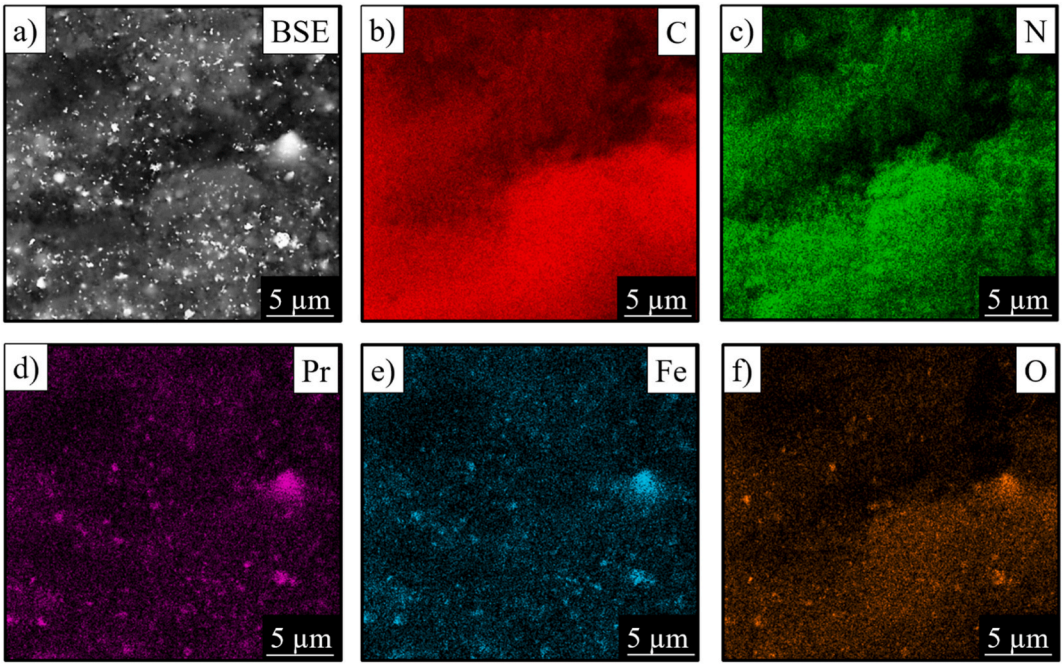

Fig. 4. Backscattered electron (BSE) image of the CN/5%PFO nanocomposite (a) and elemental mapping of the elements: C (b), N (c), Pr (d), Fe (e), O (f).

activity of the material.

3.6. Photocatalytic analysis

The photocatalytic activity of the obtained nanocomposites was evaluated during the process of decomposition of a tetracycline hydrochloride solution under the influence of visible light irradiation. The experiment with the initial CN and PFO was carried out under similar conditions for comparison. Prior to the experiment, all samples were placed in a light-tight box and mixed for 60 min to establish adsorption equilibrium in solutions. The degradation of the antibiotic in the dark experiment in the presence of catalysts was insignificant and did not exceed 3 ± 0.5 % of the initial concentration. Next, photocatalytic tests of the samples were carried out under the influence of LEDs with a wavelength of 405 nm. Typical absorption spectra of a TCHCl solution by a nanocomposite that were taken at intervals of 5 min are shown in Fig. S1. C/C_0 dependencies presented in Fig. 8 a report that pure PFO did not have sufficient photocatalytic capabilities to decompose the antibiotic under the selected conditions. This can be explained by the low values of the specific surface area and total pore volume (Table S1). At the same time, pure CN and nanocomposites based on it showed superior photoactivity. The rate constants of the TCHCl oxidation reaction were found using the kinetic equation of the pseudo-first-order reaction and arranged in the following order: CN < CN/7.5 % PFO, CN/10 % PFO < CN/2.5 % PFO < CN/5 % PFO (Fig. 8 b,c). It should be noted that the course of the graphs for the obtained samples containing 7.5 and 10 wt% of praseodymium orthoferrite differs slightly, as shown in Fig. S2. The increased photoactivity of CN/5 % PFO is explained by a combination of several factors: the low intensity of the photoluminescence spectrum, indicating a decrease in the recombination rate of electron-hole pairs (Fig. 8d), and a sufficiently high value of the specific surface area.

To better understand the obtained results, the values of TON and TOF were calculated and presented. Unlike the reaction rate constant, the calculation allows to evaluate the effectiveness of the photocatalyst while accounting for the number of active centers on its surface. Fig. 8d shows a bar chart with the obtained values for the series under study. It is shown that the values of TON and TOF increase with an increase in the mass fraction of PFO in the nanocomposite from 0 to 5 %, which is followed by a decrease in efficiency. Despite the high values of the specific surface area, the CN/7.5 % PFO and N/10 % PFO samples have low values of overall efficiency, which might be caused by reverse recombination processes. The CN/5 % PFO catalyst has an optimal ratio of the initial components, which improves light absorption and charge transfer, allowing for the effective destruction of tetracycline antibiotics in aquatic environments.

The stability of the catalyst, which showed the best results in the photocatalytic test, was measured throughout five cycles of TCHCl photodegradation under visible light irradiation. Fig. 9 shows that the 5 % CN/PFO sample retains its photocatalytic properties after cycling (Fig. 9a). The absence of a clear decrease in photocatalytic activity indicates its high photocatalytic stability. To assess the long-term photocatalytic stability, an additional study was conducted on the reproducibility of the photocatalytic degradation of tetracycline solution under the influence of visible light. After twelve cycles, there is a decrease in efficiency by 13.3 %, which indicates excellent reproducibility and durability of the studied catalyst (Fig. 9b).

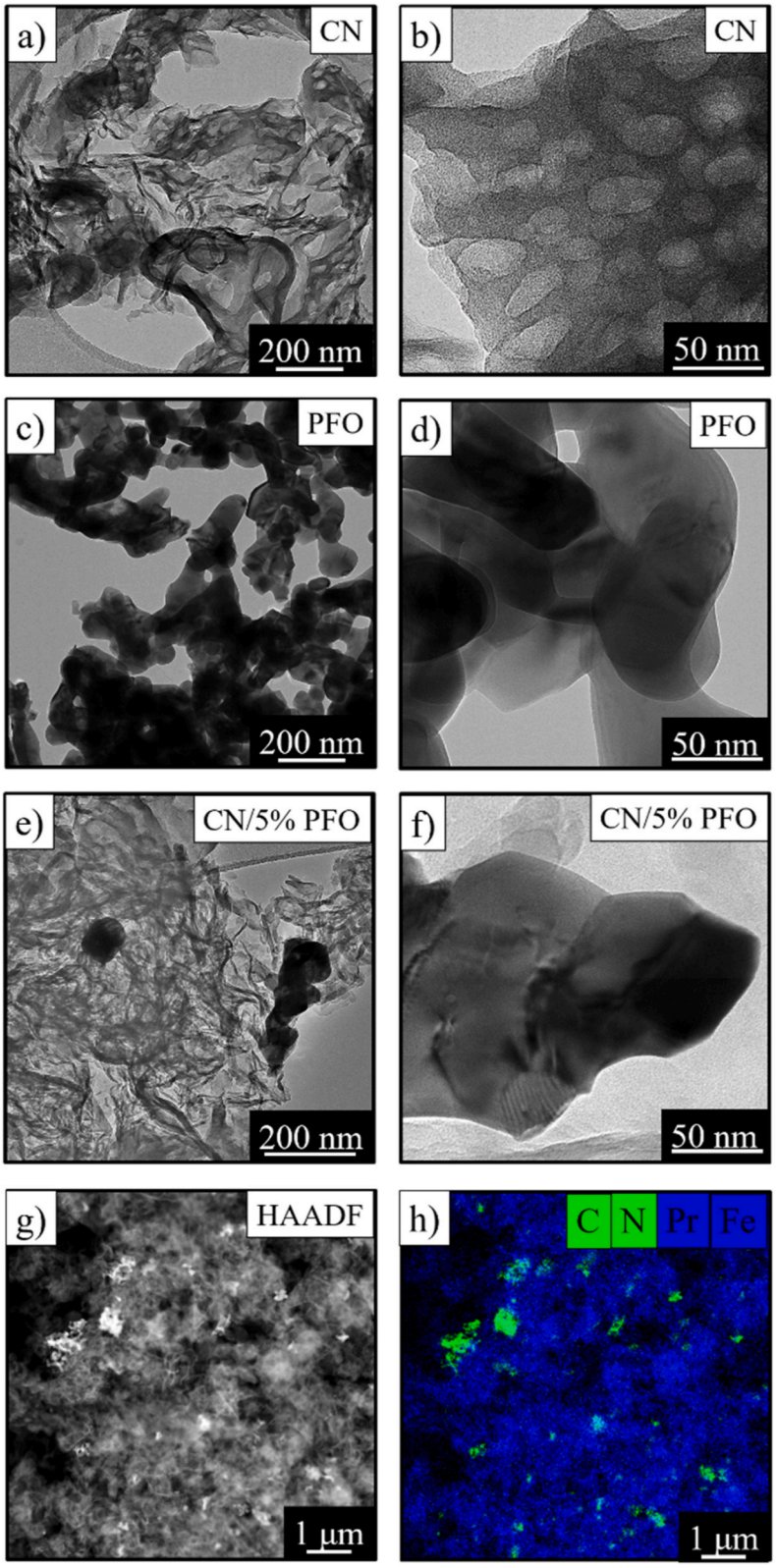

Fig. 5. TEM images of the CN (a–b), PFO (c–d), CN/5%PFO (e–f) and TEM-EDX elemental maps of CN/5%PFO (g–h) nanopowders.

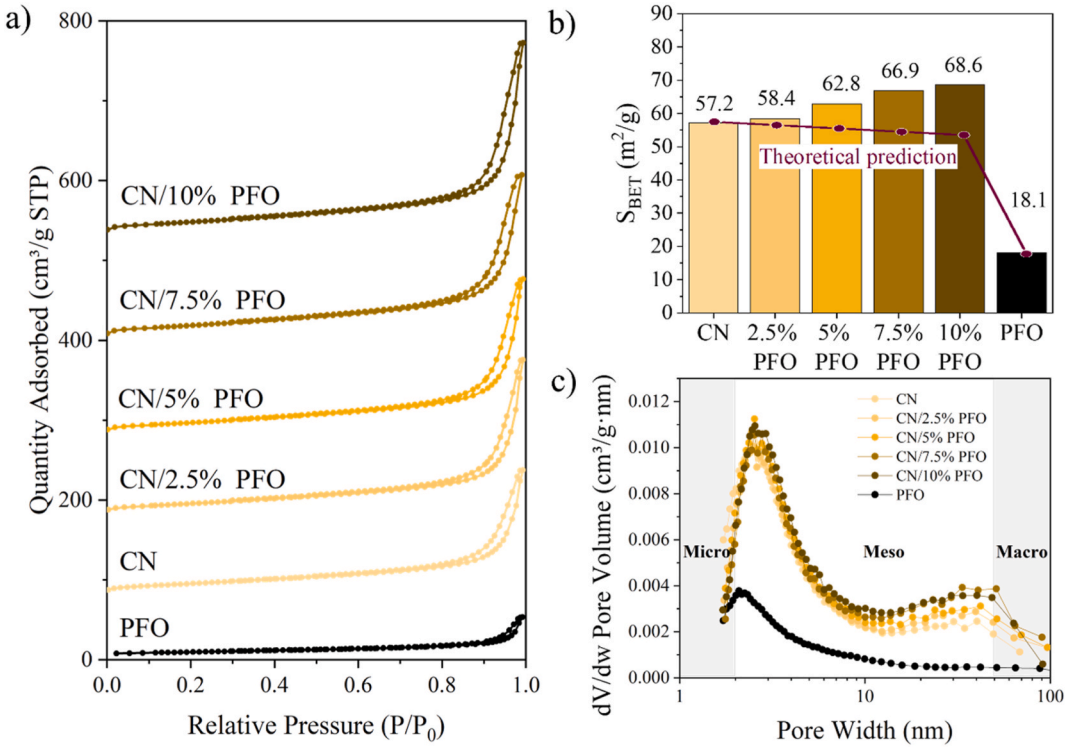

Fig. 6. Nitrogen adsorption-desorption isotherms (a), BET specific surface areas (b) and BJH pore size distribution plots (c) of the CN, PFO and CN/PFO nanocomposites.

Photocatalytic performance of CN/5 % PFO sample was further examined in the presence of different ionic species as well as wider range of catalyst dosage, results are shown on Fig. 10. Catalytic dosage (Fig. 10a and b) significantly affects the rate of photodecomposition of TCHCl, it enhanced with increase of dosage. The effect in activity is more prominent for the change from 0.5 to 1 mg and diminishes for additional 0.5 mg change (1.5 mg plot), nevertheless additional surface display itself in dark phase of experiment, by notable drop in concentration due to adsorption of TCHCl, that was negligible for previous experiments. It is known, that presence of coexisting ions can negatively affect photocatalytic performance [35,36], thus a number of tests were conducted with 1.0 mg of CN/5 % PFO sample in presence of variety of 0.1 M solutions of different inorganic salts (Fig. 10c,d,e,f). For evaluation of anionic affect, sodium chloride, nitrate and sulfate were utilized. As expected, TCHCl removal efficiency was reduced in all cases, for chloride and sulfate the effect was more prominent than for nitrate as shown on Fig. 10c and d. For cationic influence evaluation, sulfates of sodium, magnesium and zinc were used. The results (Fig. 10e and f) reveal similar decline in photoactivity of catalyst in the presents of ions. In this test zinc ion is the less active towards catalytic inhibition, sodium and magnesium showed similar results.

Tests of catalytic materials with the participation of scavenging agents were carried out to better understand the mechanism of photocatalytic degradation of an antibiotic under the influence of visible light. IPA, AA and FA were used in the experiment as agents for catching radicals. The values of the efficiency of removing TCHCl using a CN/5%PFO (Blank) photocatalyst in the presence of scavengers are shown in Fig. 11. It is shown that the addition of ascorbic acid reduces the efficiency of photocatalytic decomposition of TCHCl by 30 %, isopropanol by 21 %, and formic acid by 19 %. This suggests that all active particles (O^{2-},·OH, h^+) are critically important for the process of photocatalysis, but O^{2-} plays the primary role in this system.

It is known that photocatalysts forming type II heterojunctions and photocatalysts operating according to the Z-scheme have a similar structure but differ in the charge transfer mechanism. In the photocatalytic process, the semiconductor material must have sufficient oxidation potential to generate hydroxyl radicals and sufficient reduction potential to create superoxide radicals [37]. In particular, CN is a well-known reduction photocatalyst, while PFO is an oxidation photocatalyst. Based on the results of the photocatalytic test for the capture of radical groups, the formation of $\cdot O^{2-}$, ·OH and h^+ was recorded. However, type II heterojunction photocatalysts with low redox ability can generate only one type of radicals [38–42]. Therefore, the mechanism described below is based on the assumption that the decfomposition of TCHCl by a photocatalytic CN/5%PFO material under the action of visible light corresponds to the Z-scheme (Fig. 12).

Step 1. When a quantum of light is absorbed by CN and PFO particles, elementary charge carriers are formed, which are free electrons (ē) and electron vacancies (h^+):

$$CN + h\nu \rightarrow \bar{e} + h^+$$

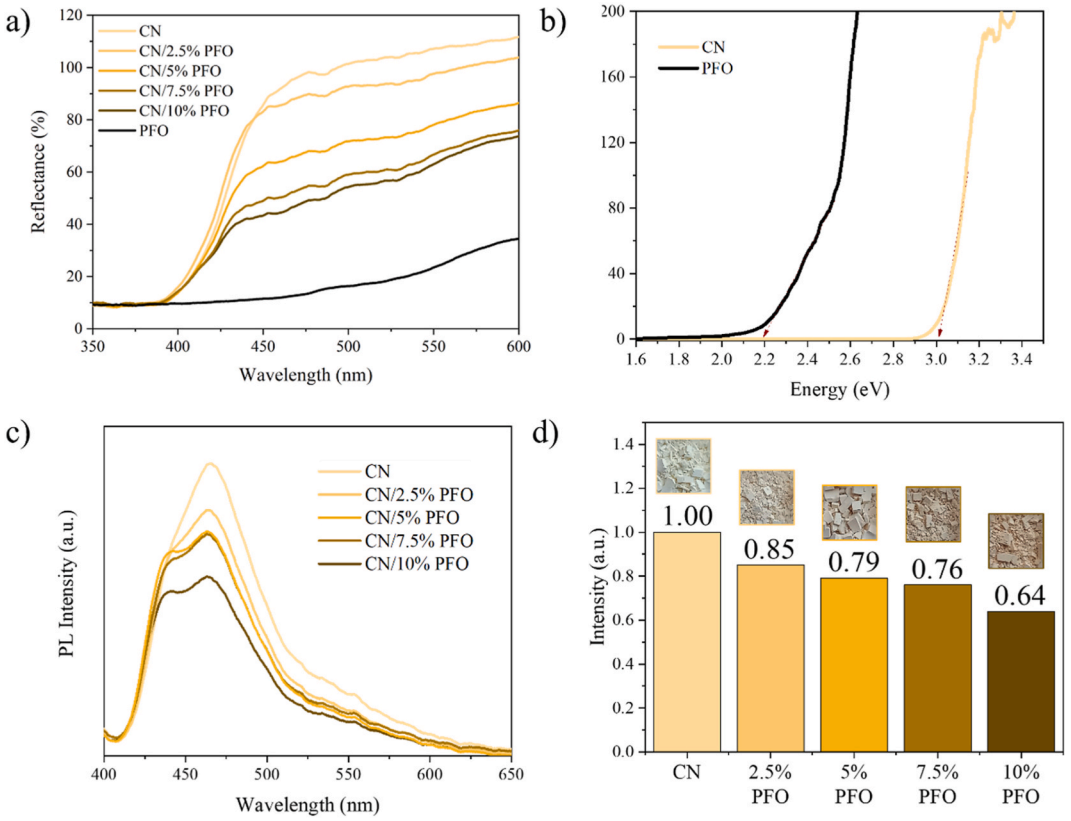

Fig. 7. UV–visible spectra (a), Kubelka-Munk functions (b) and band gap energies (c) and PL spectra (d) of the CN, PFO and CN/PFO nanocomposites.

$$PFO + h\nu \rightarrow \bar{e} + h^{+}$$

Step 2. As a result of light excitation, electrons pass from the conduction band (CB) PFO to photoexcited electron vacancies in the valence band (VB) CN. CB_{CN} electrons restore molecular oxygen and form a superoxide radical ($E_{CB} = -1.36$ eV), while E_{VB} PFO allows to react with hydroxide ions to form a hydroxyl radical:

$$\bar{e}_{(CN)} + O_2 \rightarrow \cdot O_2^-$$

$$h^+_{(PFO)} + OH^- \rightarrow \cdot OH$$

Step 3. The formed active radicals effectively oxidize TCHCl to form harmless products:

$$\left.\begin{matrix} \cdot O_2^- \\ \cdot OH \end{matrix}\right\} + TCHCl \rightarrow Products + CO_2 + H_2O$$

4. Conclusions

In conclusion, a composite photocatalyst based on graphite-like carbon nitride and praseodymium orthoferrite was successfully obtained. The series consisted of six samples: pure CN, CN/2.5 % PFO, CN/5 % PFO, CN/7.5 %, CN/10 % PFO and pure PFO. The resulting series of samples was characterized in detail using a complex of physico-chemical methods. Using X-ray phase analysis (XRD) of nanocomposites, the main crystal structure of g-C_3N_4 and the impurity phase of $PrFeO_3$ with a cubic structure were revealed. The phase purity of the initial powders of graphite-like carbon nitride and praseodymium orthoferrite was also confirmed. The chemical composition of the surface was confirmed by X-ray photoelectron spectroscopy. The morphology of powders characteristic of g-C_3N_4

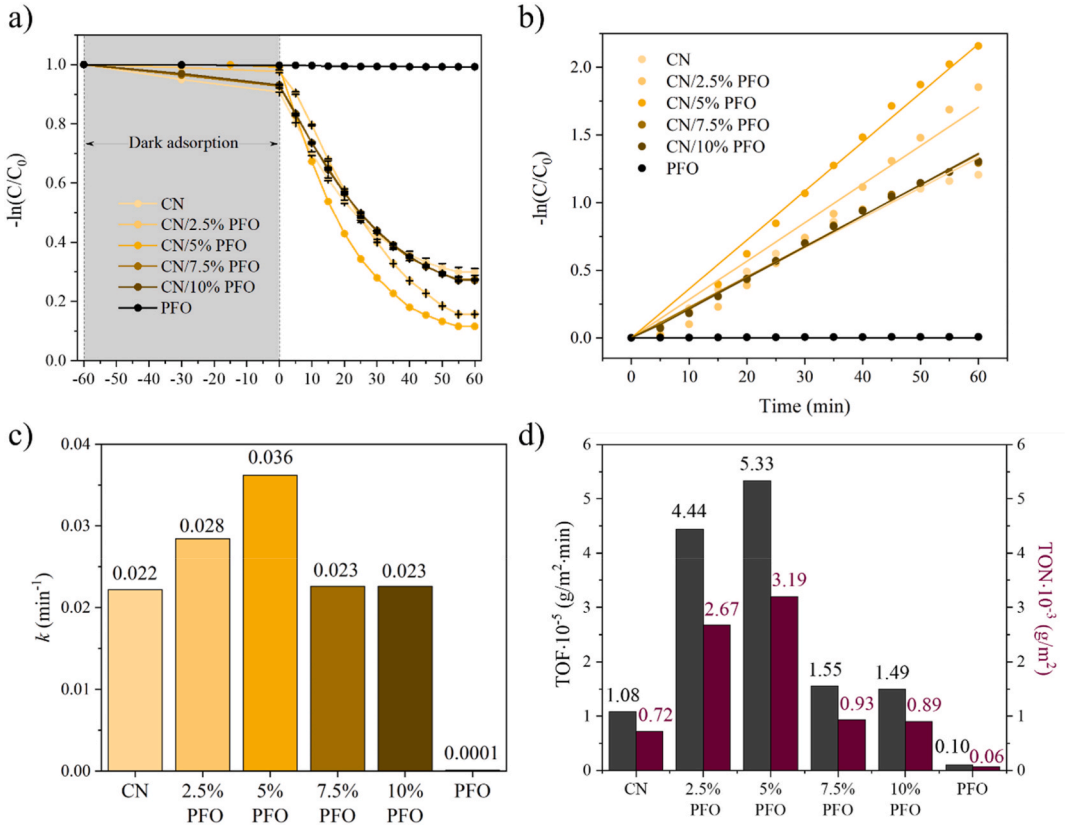

Fig. 8. Kinetics of photocatalytic degradation of TCHCl under visible light irradiation (a), pseudo-first-order reaction kinetic fitted curves (b), apparent rate constants for tetracycline degradation (c) and TOF and TON values (d) of the CN, PFO and CN/PFO nanocomposites.

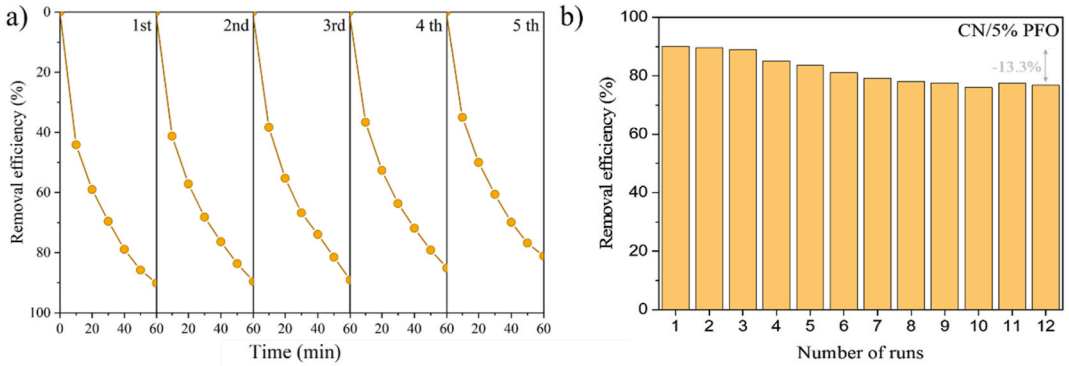

Fig. 9. Recycling stability (a) and long-term stability (b) tests of the CN/5%PFO nanocomposite for TCHCl degradation.

and $PrFeO_3$ was illustrated using SEM and PEM methods. In addition, the uniformity of the distribution of praseodymium ferrite particles over the surface of the main phase is shown. Typical type IV isotherms with pronounced H3 type hysteresis were obtained, which indicates the presence of mesopores in the catalysts. It was found that the addition of PFO to graphite-like carbon nitride leads to an increase in the specific surface area of the sample due to the introduction of praseodymium orthoferrite particles into the interlayer space of g-C_3N_4. The process of photocatalytic degradation of antibiotics under visible light irradiation was considered using the example of tetracycline hydrochloride. It was established that the obtained nanocomposites have superior photocatalytic activity and stability when reused. The optimal PFO content in the main material was determined to be 5 %. The synergistic interaction between the initial components was achieved due to numerous active centers on the developed surface of graphite-like carbon nitride and a decrease in the recombination rate of electron-hole pairs with praseodymium orthoferrite. Consequently, a possible mechanism of photocatalytic degradation in the presence of the studied catalysts that proceeds in accordance with the Z-scheme is proposed. The

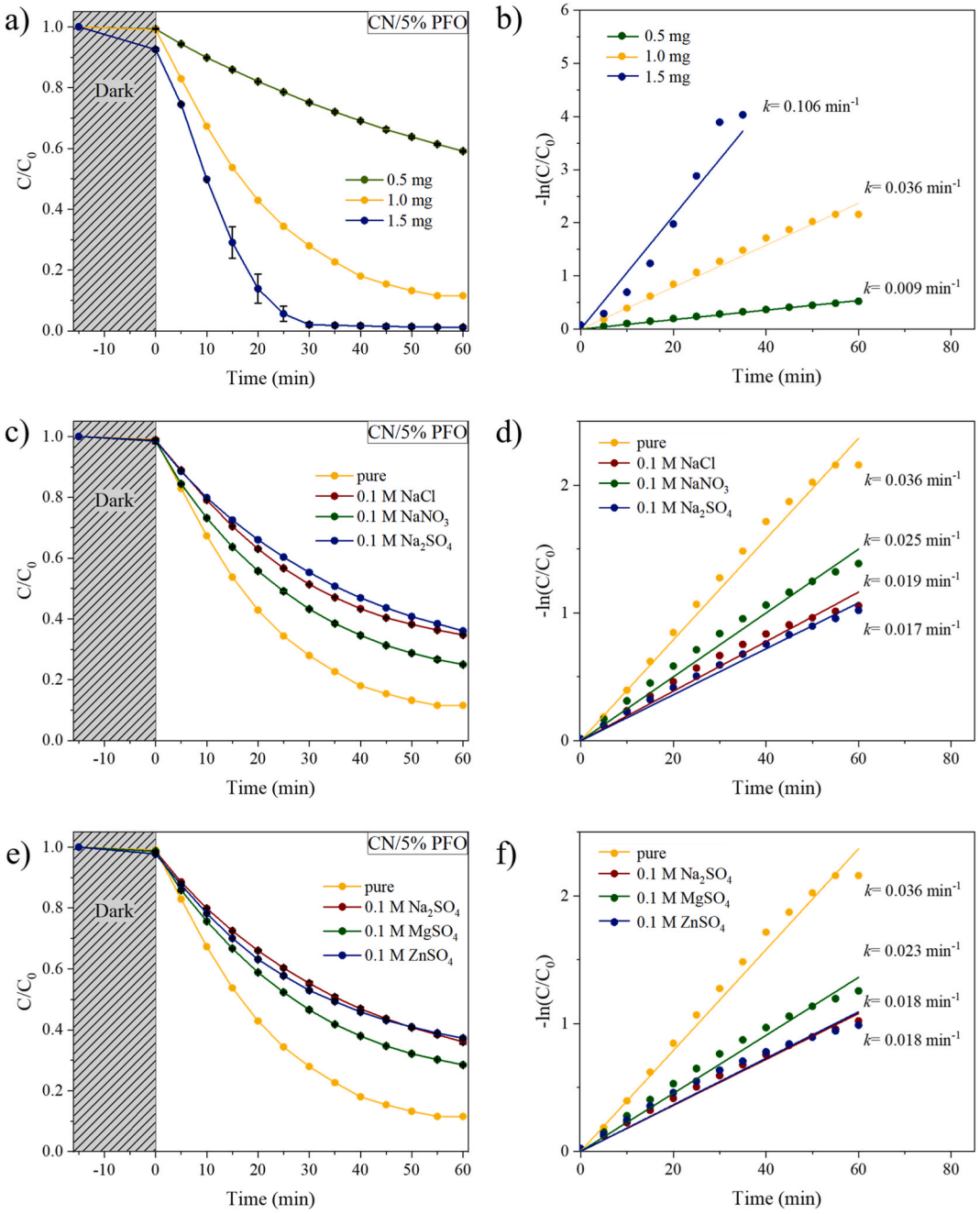

Fig. 10. Photodegradation of TCHCl and kinetic plots under various conditions (a) and (b) catalyst amount variation; (c) and (d) variety of anionic types; (e) and (f) variety of cationic types.

technique of creating a CN/PFO-based heterojunction presented in this work can be widely used in the production of inexpensive and environmentally friendly photocatalysts of the visible radiation range for the removal of dangerous pollutants from pharmaceutical wastewater.

Data availability statement

The data related to this study has not been deposited into a publicly available repository. The data that support the findings of this study are available from the corresponding author, Maria I. Chebanenko, upon request.

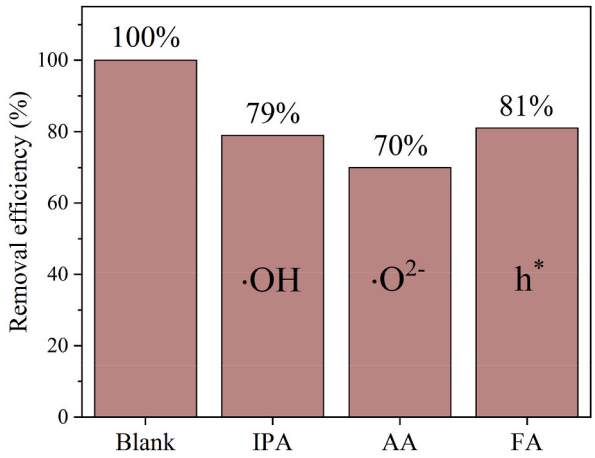

Fig. 11. Effect of radical scavengers on the photocatalytic degradation of TCHCl in the presence of g-C_3N_4/5%PFO photocatalyst.

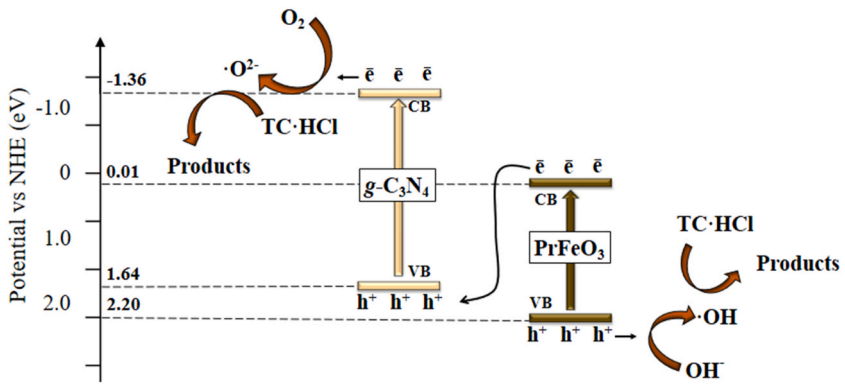

Fig. 12. Schematic representation of the Z-scheme photocatalytic mechanism.

CRediT authorship contribution statement

M.I. Chebanenko: Conceptualization, Data curation, Formal analysis, Investigation, Methodology, Project administration, Validation, Visualization, Writing – original draft, Writing – review & editing, Funding acquisition. **L.A. Lebedev:** Formal analysis, Investigation, Methodology, Software. **A.S. Seroglazova:** Conceptualization, Formal analysis, Investigation, Visualization. **A.A. Lobinsky:** Data curation, Investigation. **E.Y. Gerasimov:** Investigation, Visualization. **E. Yu Stovpiaga:** Data curation, Investigation. **V.I. Popkov:** Conceptualization, Formal analysis, Resources, Supervision, Validation.

Declaration of competing interest

The authors declare the following financial interests/personal relationships which may be considered as potential competing interests:M.I. Chebanenko reports financial support was provided by Russian Science Foundation.

Acknowledgements

This work was supported by the Russian Science Foundation (project No 23-23-00328). The authors acknowledge to the Centers for Physical Methods of Surface Investigation of Saint-Petersburg State University.

Appendix A. Supplementary data

Supplementary data to this article can be found online at https://doi.org/10.1016/j.heliyon.2023.e22038.

References

[1] M.A. Shannon, P.W. Bohn, M. Elimelech, J.G. Georgiadis, B.J. Marin, A.M. Mayes, Science and technology for water purification in the coming decades, Nature 452 (2008) 301–310, https://doi.org/10.1038/nature06599.

[2] M. Nasrollahzadeh, M. Sajjadi, S. Iravani, R.S. Varma, Green-synthesized nanocatalysts and nanomaterials for water treatment: current challenges and future perspectives, J. Hazard Mater. (2020), 123401, https://doi.org/10.1016/j.jhazmat.2020.123401.

[3] E. Yazdankish, M. Foroughi, M. Hossein, A. Azqhandi, Capture of I 131 from medical-based wastewater using the highly effective and recyclable adsorbent of g-C_3N_4 assembled with Mg-Co-Al-layered double hydroxide, J. Hazard Mater. 389 (2020), 122151, https://doi.org/10.1016/j.jhazmat.2020.122151.

[4] L. Zhang, M. Ou, H. Yao, Z. Li, D. Qu, F. Liu, J. Wang, J. Wang, Z. Li, Electrochimica Acta Enhanced supercapacitive performance of graphite-like C_3N_4 assembled with NiAl-layered double hydroxide, Electrochim. Acta 186 (2015) 292–301, https://doi.org/10.1016/j.electacta.2015.10.192.

[5] S. Nayak, L. Mohapatra, K. Parida, Visible light-driven novel g-C_3N_4/NiFe-LDH composite photocatalyst with enhanced photocatalytic activity towards water oxidation and reduction reaction, J. Mater. Chem. A (2015) 1, https://doi.org/10.1039/C5TA05002B. –14.

[6] M.I. Chebanenko, V.I. Popkov, H. Schröettner, A.A. Sushnikova, A.A. Rempel, A.A. Valeeva, Sorption-photocatalytic performance of NbO_x nanocrystals synthesized via heat-stimulated oxidation of niobium carbide, Appl. Surf. Sci. 582 (2022), https://doi.org/10.1016/j.apsusc.2022.152422, 1–9.

[7] Z. Mo, X. She, Y. Li, L. Liu, L. Huang, Z. Chen, Q. Zhang, H. Xu, H. Li, Synthesis of g-C_3N_4 at different temperatures for superior visible/UV photocatalytic performance and photoelectrochemical sensing of MB solution, RSC Adv. 5 (2015) 101552–101562, https://doi.org/10.1039/C5RA19586A.

[8] A. Kharlamov, M. Bondarenko, G. Kharlamova, N. Gubareni, Features of the synthesis of carbon nitride oxide (g-C_3N_4)O at urea pyrolysis, Diam. Relat. Mater. 66 (2016) 16–22, https://doi.org/10.1016/j.diamond.2016.03.012.

[9] N. Chidhambaram, K. Ravichandran, Single step transformation of urea into metal-free g-C_3N_4 nanoflakes for visible light photocatalytic applications, Mater. Lett. 207 (2017) 44–48, https://doi.org/10.1016/j.matlet.2017.07.040.

[10] M. Elshafie, S.A. Younis, P. Serp, E.A.M. Gad, Preparation characterization and non-isothermal decomposition kinetics of different carbon nitride sheets, Egypt, J. Petrol. 29 (2019) 21–29, https://doi.org/10.1016/j.ejpe.2019.09.003.

[11] F. Dong, L. Wu, Y. Sun, M. Fu, Z. Wu, S.C. Lee, Efficient synthesis of polymeric g-C_3N_4 layered materials as novel efficient visible light driven photocatalysts, J. Mater. Chem. 21 (2011) 15171–15174, https://doi.org/10.1039/C1JM12844B.

[12] K. Maeda, X. Wang, Y. Nishihara, D. Lu, M. Antonietti, K. Domen, Photocatalytic Activities of Graphitic Carbon Nitride Powder for Water Reduction and Oxidation under Visible Light, 2009, pp. 4940–4947, https://doi.org/10.1021/jp809119m.

[13] J. Zhang, Q. Zhu, L. Wang, M. Nasir, g-C_3N_4/CoAl-LDH 2D/2D hybrid heterojunction for boosting photocatalytic hydrogen evolution, Int. J. Hydrogen Energy 45 (41) (2020) 21331–21340, https://doi.org/10.1016/j.ijhydene.2020.05.171.

[14] Q. Shi, J. Huang, Y. Yang, J. Wu, J. Shen, X. Liu, A. Sun, Z. Liu, In-situ construction of urchin-like hierarchical g-C_3N_4/NiAl-LDH hybrid for efficient photoreduction of CO_2, Mater. Lett. 268 (2020), 127560, https://doi.org/10.1016/j.matlet.2020.127560.

[15] J. Ding, X. Lü, H. Shu, J. Xie, H. Zhang, Microwave-assisted synthesis of perovskite $ReFeO_3$ (Re: La, Sm, Eu, Gd) photocatalyst, Mater. Sci. Eng. B. 171 (2010) 31–34, https://doi.org/10.1016/j.mseb.2010.03.050.

[16] T. Chen, Z. Zhou, Y. Wang, Sensors and Actuators B : chemical surfactant CATB-assisted generation and gas-sensing characteristics of $LnFeO_3$ (ln = La, Sm, Eu) materials, Sensors Actuators, B Chem. 143 (2009) 124–131, https://doi.org/10.1016/j.snb.2009.09.031.

[17] Y. Subramanian, V. Ramasamy, R.J. Karthikeyan, G. Raj, D. Arulmozhi, R. Kumar, M. Sriramalu, Heliyon Investigations on the enhanced dye degradation activity of heterogeneous $BiFeO_3$ – $GdFeO_3$ nanocomposite photocatalyst, Heliyon 5 (6) (2019), https://doi.org/10.1016/j.heliyon.2019.e01831.

[18] A.S. Seroglazova, L.A. Lebedev, M.I. Chebanenko, A.S. Sklyarova, I. V Buryanenko, V.G. Semenov, V.I. Popkov, Ox/Red-controllable combustion synthesis of foam-like $PrFeO_3$ nanopowders for effective photo-Fenton degradation of methyl violet, Adv. Powder Technol. 33 (2022), 103398, https://doi.org/10.1016/j.apt.2021.103398.

[19] K. Rusevova, R. Köferstein, M. Rosell, H.H. Richnow, F. Kopinke, A. Georgi, $LaFeO_3$ and $BiFeO_3$ perovskites as nanocatalysts for contaminant degradation in heterogeneous Fenton-like reactions 239 (2014) 322–331, https://doi.org/10.1016/j.cej.2013.11.025.

[20] S.M. Tikhanova, L.A. Lebedev, K.D. Martinson, M.I. Chebanenko, I.V. Buryanenko, V.G. Semenov, V.N. Nevedomskiy, V.I. Popkov, The synthesis of novel heterojunction h-$YbFeO_3$/o-$YbFeO_3$ photocatalyst with enhanced Fenton-like activity under visible-light, New J. Chem. 45 (2021) 1541–1550, https://doi.org/10.1039/D0NJ04895J.

[21] F. Sarikhani, A. Zabardasti, A. Reza, S. Mahmoud, Enhanced visible light activity of $EuFeO_3$/TiO_2 nanocomposites prepared by thermal treatment – hydrolysis precipitation method, Appl. Phys. A. 126 (6) (2020) 476, https://doi.org/10.1007/s00339-020-03593-4.

[22] A.A. Ismail, I. Abdelfattah, M.F. Atitar, L. Robben, H. Bouzid, S.A. Al-sayari, D.W. Bahnemann, Photocatalytic degradation of imazapyr using mesoporous Al_2O_3-TiO_2 nanocomposites, Sep. Purif. Technol. 145 (2015) 147–153, https://doi.org/10.1016/j.seppur.2015.03.012.

[23] J. Mu, B. Chen, M. Zhang, Z. Guo, P. Zhang, Z. Zhang, Y. Sun, C. Shao, Y. Liu, Enhancement of the visible-light photocatalytic activity of In_2O_3−TiO_2 nanofiber heteroarchitectures, ACS Appl. Mater. Interfaces 3 (2012) 2, https://doi.org/10.1021/am201499r. –8.

[24] M. Zhang, X. Zhao, Y. Dong, Ch Hu, X. Xiang, X. Zeng, J. Jia, Ch Jin, L. Ding, X. Chen, In-situ synthesis of 0D/1D CeO_2/$Zn_{0.4}Cd_{0.6}S$ S-scheme heterostructures for boosting photocatalytic remove of antibiotic and chromium, Ceram. Int. 49 (2023) 5842–5853, https://doi.org/10.1016/j.ceramint.2022.11.256.

[25] Ch-X. Xu, Y.-L. Kong, W.-J. Zhang, M.-D. Yang, K. Wang, L. Chang, W. Chen, G.-B. Huang, J. Zhang, S-scheme 2D/2D $FeTiO_3$/g-C_3N_4 hybrid architectures as visible-light-driven photo-Fenton catalysts for tetracycline hydrochloride degradation, Separ. Purif. Technol. 303 (2022), 122266, https://doi.org/10.1016/j.seppur.2022.122266.

[26] S. Shi, J. Xu, L. Li, Preparation and photocatalytic activity of ZnO nanorods and ZnO/Cu_2O nanocomposites, Main Group Chem. 16 (2017) 47–55, https://doi.org/10.3233/MGC-160224.

[27] M.I. Chebanenko, S.O. Omarov, A.A. Lobinsky, V.N. Nevedomskiy, V.I. Popkov, Steam exfoliation of graphitic carbon nitride as efficient route toward metal-free electrode materials for hydrogen production, Int. J. Hydrogen Energy 48 (71) (2023) 27671–27678, https://doi.org/10.1016/j.ijhydene.2023.03.468.

[28] M.I. Chebanenko, N. V Zakharova, A.A. Lobinsky, V.I. Popkov, Ultrasonic-Assisted exfoliation of graphitic carbon nitride and its electrocatalytic performance in process of ethanol, Reforming 53 (2019) 2072, https://doi.org/10.1134/S106378261912008X. –2077.

[29] M.I. Chebanenko, N.V. Zakharova, V.I. Popkov, Synthesis and visible-light photocatalytic activity of graphite-like carbon nitride nanopowders, Russ. J. Appl. Chem. 93 (4) (2020) 494–501, https://doi.org/10.1134/S1070427220040035.

[30] B. Yalcin, S. Ozcelik, K. Icin, K. Senturk, B. Ozcelik, L. Arda, Structural , optical , magnetic , photocatalytic activity and related biological effects of $CoFe_2O_4$ ferrite nanoparticles, J. Mater. Sci. Mater. Electron. 32 (2021) 13068–13080, https://doi.org/10.1007/s10854-021-05752-6.

[31] W. Zhang, Y. Ma, X. Zhu, S. Liu, T. An, J. Bao, X. Hu, H. Tian, Fabrication of Ag decorated g-C_3N_4/$LaFeO_3$ Z-scheme heterojunction as highly efficient visible-light photocatalyst for degradation of methylene blue and tetracycline hydrochloride, J. Alloys Compd. 864 (2021), 158914, https://doi.org/10.1016/j.jallcom.2021.158914.

[32] F. Qiao, J. Wang, Sh Ai, L. Li, As a new peroxidase mimetics: the synthesis of selenium doped graphitic carbon nitride nanosheets and applications on colorimetric detection of H_2O_2 and xanthine, Sens. Actuators, B 216 (2015) 418–427, https://doi.org/10.1016/j.snb.2015.04.074.

[33] V. Alman, · K. Singh, · T. Bhat, · A. Sheikh, · S. Gokhale, Sunlight Assisted improved photocatalytic degradation of rhodamine B using Pd-loaded g-C_3N_4/WO_3 nanocomposite, Appl. Phys. A 126 (2020) 724, https://doi.org/10.1007/s00339-020-03914-7.

[34] B. Jiang, L. Li, Q. Zhang, J. Ma, H. Zhang, K. Yu, Zh Bian, X. Zhang, X. Ma, D. Tang, Iron–oxygen covalency in perovskites to dominate syngas yield in chemical looping partial oxidation, J. Mater. Chem. A 9 (2021) 13008–13018, https://doi.org/10.1039/D1TA02103F.

[35] M. Zhang, Y. Dong, M. Peng, X. Chen, Q. Zheng, J. Liao, W. Chen, Band gap-controllable N, P co-doped carbon@$Zn_xCd_{1-x}In_2S_4$ for photocatalytic reduction of chromium(VI) and degradation of tetracycline hydrochloride, Separ. Purif. Technol. 322 (2023), 124294, https://doi.org/10.1016/j.seppur.2023.124294.

[36] H. Yang, Z.-C. Zhao, Y.-P. Yang, Zh Zhang, W. Chen, R.-Q. Yan, Y. Jin, J. Zhang, Defective WO_3 nanoplates controllably decorated with MIL-101(Fe) nanoparticles to efficiently remove tetracycline hydrochloride by S-scheme mechanism, Separ. Purif. Technol. 300 (2022), 121846, https://doi.org/10.1016/j.seppur.2022.121846.

[37] G. Liao, C. Li, X. Li, B. Fang, Review Emerging polymeric carbon nitride Z-scheme systems for photocatalysis, Cell Reports Phys. Sci. 2 (2021), 100355, https://doi.org/10.1016/j.xcrp.2021.100355.
[38] J. Fernández-catalá, R. Greco, M. Navlani-garcía, W. Cao, Á. Berenguer-Murcia, g-C_3N_4 -based direct Z-scheme photocatalysts for environmental applications, Catalysts 12 (10) (2022) 1137, https://doi.org/10.3390/catal12101137.
[39] H. Yin, C. Yuan, L. Huijun, K. Zhang, X. Chen, Y. Zhang, Yo Zhang, Fabrication of 2D/1D Bi_2WO_6/C_3N_5 heterojunctions for efficient antibiotics removal, Powder Technol. 413 (2022), 118083, https://doi.org/10.1016/j.powtec.2022.118083.
[40] M. Zhang, M. Arif, Y. Dong, X. Chen, X. Liu, Z-scheme TiO2−x@ZnIn2S4 architectures with oxygen vacancies-mediated electron transfer for enhanced catalytic activity towards degradation of persistent antibiotics, J. Col. Surf. 649 (2022), 129530, https://doi.org/10.1016/j.colsurfa.2022.129530.
[41] H. Yin, C. Yuan, L. Huijun, K. Zhang, X. Chen, Yo Zhang, The interface design of (0D/2D/1D) AgI/BiOI/C_3N_5 dual Z-scheme heterostructures with efficient visible-light-driven photocatalytic activity, J. Sep. Pur. Techn. 308 (2023), 122815, https://doi.org/10.1016/j.seppur.2022.122815.
[42] H. Yin, Y. Cao, T. Fan, M. Zhang, J. Yao, P. Li, S. Chen, X. Liu, In situ synthesis of Ag_3PO_4/C_3N_5 *Z*-scheme heterojunctions with enhanced visible-light-responsive photocatalytic performance for antibiotics removal, Sci. Total Environ. 754 (2021), 141926, https://doi.org/10.1016/j.scitotenv.2020.141926.